Pure appl. geophys. 166 (2009) 869–898
0033–4553/09/050869–30
DOI 10.1007/s00024-009-0493-2



Pure and Applied Geophysics

# Compaction and Failure in High Porosity Carbonates: Mechanical Data and Microstructural Observations

P. Baud,[1] S. Vinciguerra,[2] C. David,[3] A. Cavallo,[2] E. Walker,[1] and T. Reuschlé[1]

*Abstract*—We investigated systematically the micromechanics of compaction in two carbonates of porosity above 30%, Majella grainstone and Saint Maximin limestone. The composition, grain size and pore surface area of these rocks were determined. Hydrostatic compression experiments were performed under dry and wet conditions beyond the onset of grain crushing. A significant water weakening effect was observed in both rocks. A set of conventional triaxial experiments was also performed on both rocks under dry conditions at confining pressures ranging from 3 to 31 MPa. Microstructural observations were carried out on the deformed samples. The mechanical behavior of these high porosity carbonates is dominated by shear-enhanced compaction associated in most cases with strain hardening. Stress-induced cracking and grain crushing are the dominant micromechanisms of deformation in both rocks. In Majella grainstone, compactive shear bands appeared at low confinement, in qualitative agreement with the deformation bands observed in the field. At higher confining pressures, compaction localization was inhibited and homogeneous cataclastic flow developed. In Saint Maximin limestone, compaction localization was observed at all confining pressures. An increasing number of compactive shear bands at various orientations appeared with increasing strain. These new data suggest that compaction localization is important in the mechanical compaction of high porosity carbonates.

**Key words:** High porosity carbonates, triaxial deformation, microstructural observations, microcracking, compaction localization.

## 1. Introduction

Compactive and dilatant deformation in porous rocks is a crucial problem in fault development, geotechnical engineering and reservoir/aquifer management. Active tectonics and extraction of hydrocarbons and groundwater modify the pore pressure in a reservoir/aquifer, causing variations of the effective stress possibly leading to faulting and inelastic deformation. The ability to interpret and predict the occurrence and extent of

[1] Institut de Physique du Globe de Strasbourg (UMR 7516 CNRS, Université de Strasbourg/EOST), 5 rue René Descartes, 67084 Strasbourg Cedex, France. E-mail: patrick.baud@eost.u-strasbg.fr

[2] Istituto Nazionale di Geofisica e Vulcanologia, Sezione di Roma1, via di Vigna Murata 605, 00143 Rome, Italy. E-mail: Sergio.vinciguerra@ingv.it.

[3] Université de Cergy-Pontoise, 5 mail Gay-Lussac, Neuville-sur-Oise, 95031 Cergy-Pontoise Cedex, France.

such deformation depends on a fundamental understanding of inelastic behavior, failure mode and brittle-ductile transition in porous rocks.

Numerous studies have described mechanical compaction in porous silicate rocks (Handin and Hager, 1957; Hadizadeh and Rutter, 1983; Baud *et al.*, 2004). At room temperature, the failure mode evolves with increasing pressure from brittle fracture to either cataclastic flow or more complex failure modes (Wong *et al.*, 1997). In the brittle regime, stress-induced dilatancy precedes the development of macroscopic fractures (Brace, 1978). In the compactive regime, the pore space undergoes significant inelastic compaction while the rock strain hardens (Edmond and Paterson, 1972; Wong *et al.*, 1997; Baud *et al.*, 2006). In porous sandstone, recent studies (Wong *et al.*, 2001; Baud *et al.*, 2004; Fortin *et al.*, 2005; Tembe *et al.*, 2008) show that in many cases the rocks do not fail by cataclastic flow but by discrete compaction bands developed at the brittle-ductile transition. The different failure modes, all involving microcracking (Menéndez *et al.*, 1996; Baud *et al.*, 2004), can be recognized in the laboratory by different acoustic emission activity at the onset of inelastic deformation.

In carbonates, the brittle-ductile transition shows some different attributes. Limestones and marbles undergo the brittle to plastic transition at room temperature for confining pressures accessible in the laboratory (Robertson, 1955; Paterson, 1958; Heard, 1960; Rutter, 1974; Evans *et al.*, 1990) because calcite requires relatively low shear stresses to initiate mechanical twinning and dislocation. Many previous studies focused on the mechanical behavior of very low porosity rocks such as Carrara marble (Rutter, 1974; Fredrich *et al.*, 1989), or very porous chalks (Teufel *et al.*, 1991, Risnes *et al.*, 2005). In limestones of intermediate porosity (from 3% to 18%), a similar phenomenology of failure was observed (Baud *et al.*, 2000a; Vajdova *et al.*, 2004). Dilatancy and shear localization developed under low confining pressure, while strain-hardening and shear-enhanced compaction were observed at high confining pressure. After a certain amount of strain-hardening, the samples consistently switched from compaction to dilatancy. This phenomenology of dilatant and compactant failure is similar to that of many porous sandstones. Several micromechanical models were used to capture the interplay of dilatancy and compaction in carbonate rocks (Vajdova *et al.*, 2004). In carbonates, unlike for sandstone, because of crystal plasticity, microcracking is not always the dominant micromechanism of deformation. In the compactive regime, a model involving plastic pore collapse (Curran and Carroll, 1979) was tested to interpret the experimental data. However, this approach was unsuccessful, suggesting that macroscopic yielding is controlled by a complex interplay of cracking and crystal plasticity (Vajdova *et al.*, 2004). To date there is however a paucity of microstructural data to constrain more elaborate models.

In this study we have extended the scope of Vajdova *et al.*'s (2004) work on limestones to investigate systematically the micromechanics of compaction in two carbonates of porosity greater than 30%. We specifically focused on several related questions:

- Is the phenomenology of compaction in these very high porosity rocks similar to that of less porous limestones and silicate rocks? In Tavel and Indiana limestone, VAJDOVA *et al*. (2006) reported significant twinning and microcracking during cataclastic flow. The extent and intensity of twinning increased with increasing pressure and strain, and its coupling to microcracking can be very complicated, in particular if the pore structure is complex.
- What is the dominant micromechanism of deformation leading to macroscopic compaction in very high porosity carbonates? Unlike that for sandstone, no compaction localization has been reported in laboratory experiments on calcitic rocks. Recent field observations in porous carbonates (TONDI *et al*., 2006) suggested however that complex failure modes involving deformation bands and compaction bands could be observed in this type of rock.
- How does the starting microstructure of porous carbonates trigger or inhibit the development of compaction localization over a wide range of pressures?
- Is the weakening effect of water comparable to what has been quantified in porous sandstones (RUTTER and MAINPRICE, 1978; BAUD *et al*., 2000b)? Most recent mechanical data on porous carbonates were obtained under dry conditions.

In this paper we address these issues by presenting new mechanical data; detailed analysis of rock microstructure, and by comparing our results with the prediction of bifurcation analysis.

## 2. Petrophysical Description of the Studied Materials

### 2.1. Source of Materials

Two high porosity carbonates were selected in this study: Majella grainstone (MA) from the Madonna delle Mazze quarry in the Apennines (Central Italy) and Saint-Maximin limestone (SML) from the Rocamat quarry in Saint-Maximin-sur-Oise, north of Paris (France). The blocks of Majella considered in this study belong to the undeformed host rock outcropping in the quarry, which is situated on the inner part of the forelimb of the Majella anticline (TONDI *et al*., 2006). The petrophysical description of both rocks is summarized in Table 1.

Table 1

*Petrographic description of the rocks used in this study*

| Rock Name | Porosity (%) | Average grain radius (μm) | Origin | Composition | Specific Area ($m^2/g$) |
|---|---|---|---|---|---|
| Majella grainstone | 30 | 27 | Central Apennines (Italy) | 100% calcite | 0.15 |
| Saint-Maximin limestone | 37 | 70 | Paris (France) | 61% calcite, 39% quartz | 1.4 |

### 2.2. *Porosity, Composition, Grain and Pore Characterization*

Starting porosity was determined for both rocks using two techniques: water saturation and gas pycnometer (Accupyc 1330). Porosity values of 30% and 31% for MA and 37% and 39% for SML were respectively found, through the two techniques.

We studied the composition and the grain size of both carbonates from petrographic thin sections. Intact samples were immersed in a bath of epoxy, ground flat and polished. The thin sections were carbon-coated and analyzed with a Field Emission Gun-Scanning Electron Microscope (FESEM) and an Electronic Probe Micro Analyser (EPMA). FESEM and EPMA allowed us to semi-quantitatively analyze the chemical composition of grains over an area of about 5 $\mu m^2$. FESEM images have been collected using the backscattered electron (BSE) mode at magnification 50 to 5000. Grain size was determined from the obtained images from the mean of the minimum and maximum Feret diameters.

The semi-quantitative chemical analysis combined with the image analysis indicate that MA is a pure calcite grainstone formed from rudist bivalve fragments (Tondi *et al.*, 2006), without a preferred orientation, cast into a poorly consolidated calcite cement (Fig.1a). The grain size is widely variable from a few microns to mm-sized with an average grain diameter of $\sim$54 μm.

SML conversely shows subangular and poorly sorted grains, mainly formed by $CaCO_3$ (61%) and $SiO_2$ (39%) embedded into a calcite matrix and frequent fossils fragments (Figs. 1 b-c). Grain size variability is between 1–500 microns with an average grain diameter of $\sim$140 microns. The silica grains are slightly larger ($\sim$150 μm) than the calcite grains ($\sim$100 μm).

Pore throat statistics were determined on intact samples from mercury injection experiments using a micrometrics Autopore IV 9500. SML has a broader spectrum of pore throat sizes than Majella (see Fig. 2). A strong peak is observed for SML at 26.4 microns. In Majella, the peak value is centered at 16.2 μm and there is no pore throat with a diameter lower than 0.2 μm. The internal pore surface area of the connected porosity was measured using the BET method (Brunauer *et al.*, 1938). The pore surface area was found to be 1.4 $m^2/g$ for SML and 0.15 $m^2/g$ for Majella grainstone. Since no significant crack porosity was observed in either rock, the surface area difference is likely due to the presence of smaller particles in SML, and the grain shape and pore size distributions.

### 2.3. *Fabric Anisotropy*

The variability of physical properties was used to assess the orientation of the bedding plane in both rocks, which was not obvious from visual inspection of the blocks. P-wave velocity was measured on core samples in different directions following the method described in Louis *et al.* (2004). A set of 21 independent P-wave velocity measurements

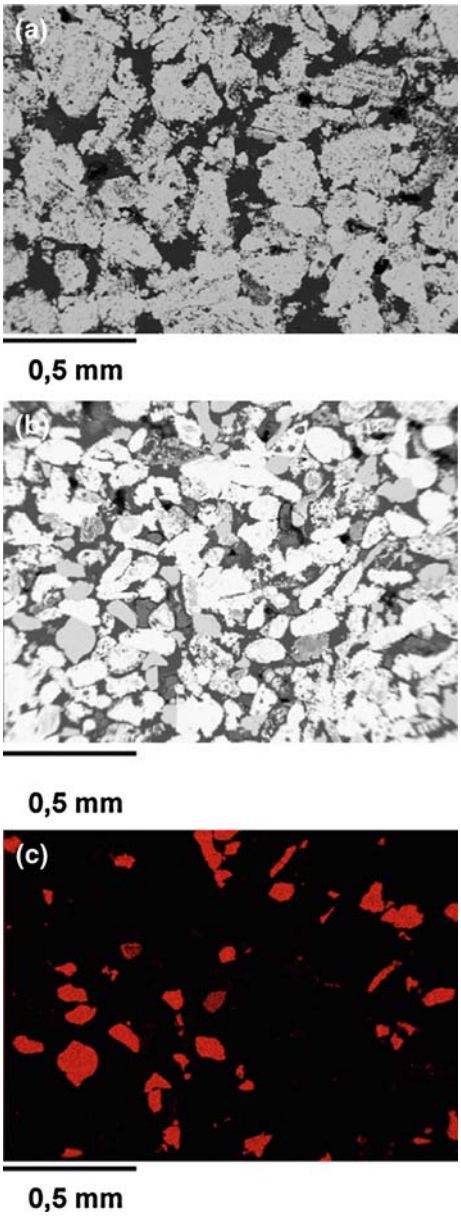


Figure 1
Micrographs of intact samples of Majella grainstone (a) and Saint Maximin limestone (b). (c) Semi-quantitative analysis of Si in SML. High Si concentrations are brighter.

was obtained on samples cored in three orthogonal directions. For each sample 8 measurements were made across diameters with an angular spacing of 22.5°. From this data set it is possible to build a second-rank velocity pseudo-tensor from which principal

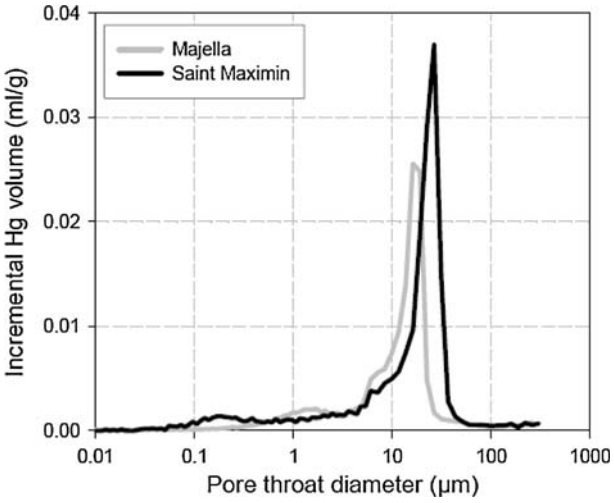


Figure 2
Pore throat statistics derived from mercury injection tests on intact samples of Majella grainstone (light grey) and Saint-Maximin limestone (dark grey).

directions can be inferred. These directions, corresponding to minimum, intermediate and maximum eigenvalues of the velocity pseudo-tensor can be compared to geological features such as bedding, strike and dip of folded structures, as well as direction and magnitude of regional stresses. These measurements were made first on dry samples, then in water saturated conditions. Figure 3 shows the evolution of P-wave velocity as a function of the measurement angle for the samples for which the largest variations were observed, for dry and wet samples of both Majella grainstone and Saint-Maximin limestone. For both rocks the velocity of the water saturated samples is systematically higher than that of the dry samples as expected. The angular velocity variations, however, are smaller in the saturated samples than the dry. This decrease in anisotropy occurs when the pore space is filled with a stiffer phase and can be interpreted as a pore shape anisotropy effect, as measured from Baud *et al.* (2005) for Bentheim sandstone and confirmed by both theoretical and microstructural studies (Louis *et al.*, 2005). Although other sources of anisotropy are possible, pore shape anisotropy might be important in both Majella and SML. Figures 3b,d show stereoplots of the orientation of the principal values for the P-wave velocities derived from the pseudo-tensor analysis on the data set corresponding to the water-saturated samples. For both rocks, the fabric is triaxial, with 3 different eigenvalues. The anisotropy factor A (Fig. 3) is calculated as the difference between maximum and minimum eigenvalues normalized to the mean velocity. For SML, the anisotropy in the saturated samples is negligible and should not have a strong influence on the mechanical behavior. However we found that A is close to 13% in dry SML.

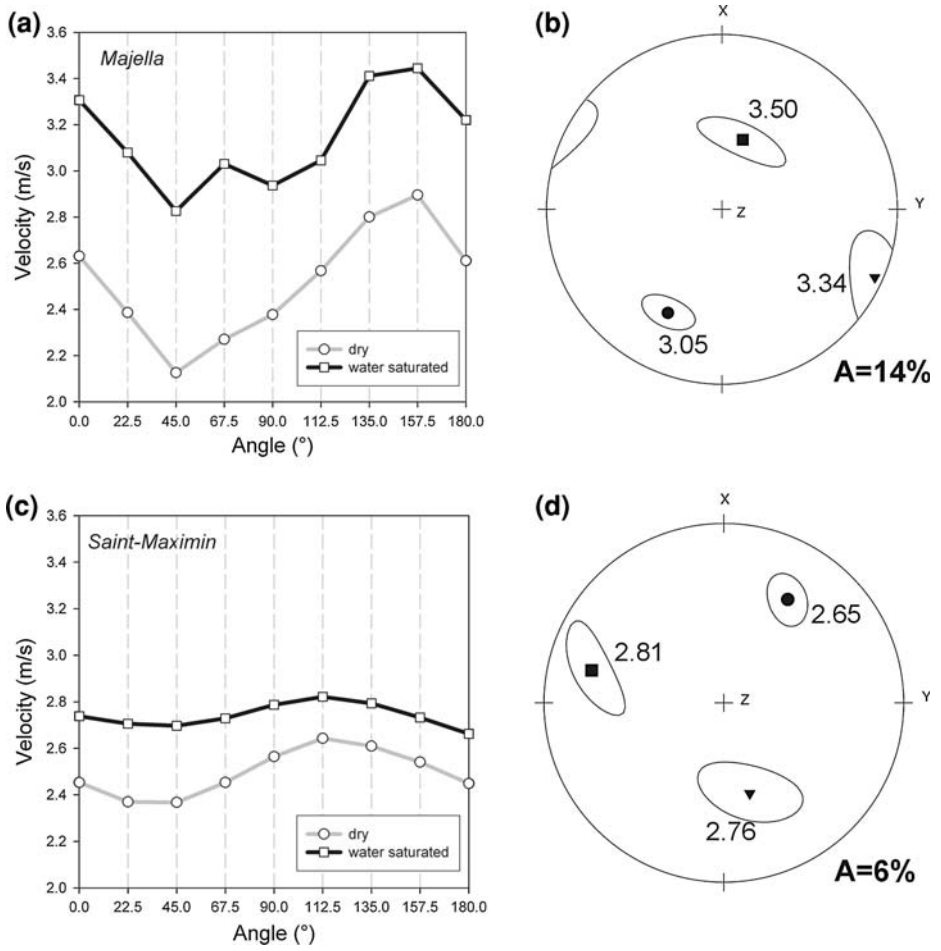


Figure 3

Evolution of P-wave velocity (a-c) across 8 different diameters in dry (circles) and water-saturated (squares) core samples for (a) Majella grainstone and (c) Saint. Maximin limestone. The directions X, Y and Z correspond to the reference frame linked to the blocks from which the core samples have been prepared. Stereoplots (b, d) with the orientation of the principal velocity values derived from the pseudo-tensor analysis with the corresponding velocity magnitude (in km/s), the 95% confidence ellipses and the anisotropy factor A for wet samples of the two rocks investigated.

### *2.4. Sample Orientation for Mechanical Tests*

The core sample axis for the mechanical tests corresponds to the Z direction for SML. Assuming that the bedding plane incorporates two of the principal directions, the direction in which the samples were cored is oblique with respect to both the bedding plane and the bedding pole. Compared to SML, the P-wave velocity anisotropy for MA is

significantly higher in both the saturated (A = 14%, Fig. 3) and the dry samples (A = 27%). The direction in which the samples for the mechanical tests were cored corresponds to the X-axis, which approaches the direction corresponding to the minimum velocity. Assuming that the minimum velocity indicates the direction perpendicular to the bedding (Baud *et al.*, 2005; David *et al.*, 2007), the direction of the core axis is almost parallel to the bedding pole for MA samples tested in the triaxial experiments. Due to the high elastic anisotropy in MA, it is expected that the behavior would be significantly influenced by anisotropic features such as bedding orientation, pore shape anisotropy or distribution of contacts between grains at a small scale.

## 3. Experimental Procedure

Cylindrical samples of 20-mm of diameter and 40-mm of length were cored in the Z direction (oblique with respect to the sedimentary bedding, see previous section) for SML and in the X direction (assumed to be almost perpendicular to bedding) for MA. Jacketed samples were deformed in conventional triaxial configuration at room temperature at École et Observatoire des Sciences de la Terre (EOST) in Strasbourg, see Klein and Reuschlé (2004) for apparatus and measurements details. Most tests were performed at confining pressures ranging from 3 to 50 MPa in nominally dry conditions. A few tests were performed on wet samples saturated with deionized water. A computer-controlled stepping motor connected to a pressure transducer regulated the confining pressure with an accuracy of 0.05 MPa. The axial load was applied by a piston controlled by a second computer-controlled stepping motor. Axial displacement was measured outside the pressure vessel with a capacitive transducer with accuracy 0.2 μm mounted on the moving piston and servo-controlled at a fixed rate (corresponding to a nominal strain rate of $10^{-5}$/s).

Hydrostatic experiments were performed at a fixed pore pressure of 10 MPa under fully drained conditions. The pore volume change was recorded by monitoring the displacement of the pore pressure generator with an angular encoder. The porosity change was calculated from the ratio of the pore volume change to the initial bulk volume of the sample. Due to the very porous and weak nature of the rocks investigated in this study, it was impossible to use strain gauges to measure axial and radial strain in the dry experiments. In all attempts, stress-induced pore-collapse resulted in breakage of the gauges even when the surfaced pores were filled with a thin layer of fast-cured epoxy. Volumetric strain was thus recorded in dry and wet tests by monitoring the piston displacement of the confining pressure generator with an angular encoder. This method was tested over the pressure range investigated in this study by comparing the volumetric signal ($\varepsilon_{kk}$) with the porosity change inferred from a comparable pore volume monitoring ($\Delta\phi$) during experiments on water-saturated samples in drained conditions. The independent regulations of pore and confining pressures lead to comparable estimations of the volumetric strain and porosity reduction: $\varepsilon_{kk} = \Delta V/V \approx \Delta\phi$. Because this method

is a measurement of the whole sample volume, the volumetric strain was not affected by strain localization.

## 4. Mechanical Data

In this paper we will use the convention that the compressive stresses and compactive strains (i.e., shortening and porosity decrease) are considered positive. We will denote the maximum and minimum (compressive) principal stresses by $\sigma_1$ and $\sigma_3$, respectively. The pore pressure will be denoted by $P_p$, and the difference $P_c - P_p$ between the confining pressure ($P_c = \sigma_2 = \sigma_3$) and pore pressure will be referred to as the "effective pressure" $P_{eff}$. The effective mean stress $(\sigma_1 + 2\sigma_3)/3 - P_p$ will be denoted by $P$ and the differential stress $\sigma_1 - \sigma_3$ by $Q$.

### 4.1. Majella Grainstone

Sixteen dry and four wet experiments were performed on MA. Figure 4 presents our data for hydrostatic compaction in wet (Fig. 4a) and dry (Fig. 4b) conditions. The wet hydrostat (symbols) shows two stages; (1) an approximately linear poroelastic stage at low pressure, indicative of no significant crack porosity; and (2) a second stage showing deviation from linearity, corresponding to the onset of grain crushing and pore collapse

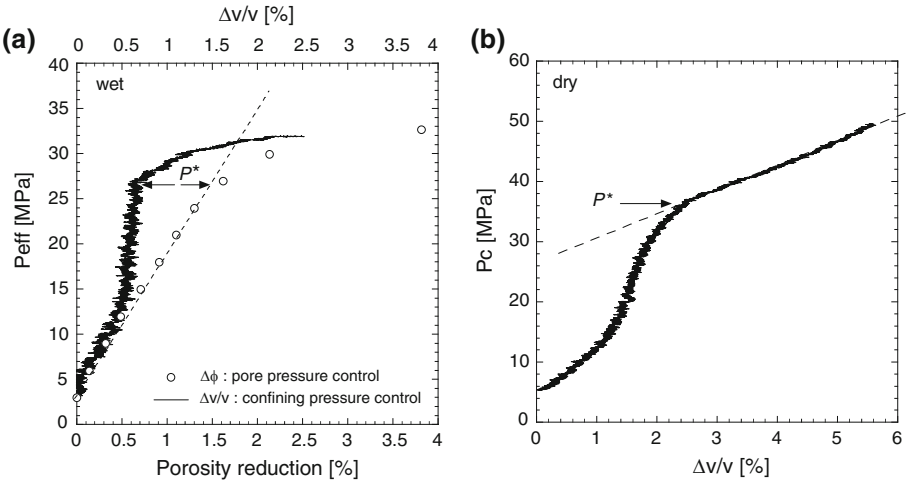


Figure 4
Representative mechanical data for hydrostatic compression experiments on Majella grainstone. (a) Effective pressure versus porosity reduction (symbols) and volumetric strain (line) for a sample deformed in wet conditions at a constant pore pressure of 10 MPa. (b) Confining pressure versus volumetric strain for a sample deformed in dry conditions. The arrow indicates the critical pressure $P^*$ for the onset of pore collapse.

(ZHANG *et al.*, 1990). The effective pressure at the transition is denoted $P^*$, which corresponds to an inflexion point in the hydrostat. The critical effective pressure $P^*$ for saturated MA was observed to be 26.5 MPa. Figure 4a also shows the volumetric response recorded from the confining pressure monitoring. When the confining pressure increased during the hydrostatic test, the calibrated volumetric strain did not match the porosity reduction. However, for a weak and compressible rock such as Majella grainstone, grain crushing and pore collapse resulted in a very strong acceleration of the compaction which appeared clearly and simultaneously on both volumetric signals from pore and confining pressure monitoring. The volumetric signal from the confinement control can therefore be used to estimate $P^*$ in dry conditions. Several dry hydrostatic tests were performed and gave comparable results. $P^*$ appeared more evident if instead of increasing the confining pressure by small steps, as was done in the wet experiment presented in Figure 4a, a very slow continuous rate was applied. A representative example is presented in Figure 4b where the confining pressure was increased at a rate of 0.001 MPa/s. $P^*$ was found to be 37 MPa in dry conditions.

Mechanical data for selected experiments performed at confining pressures ranging from 5 to 31 MPa are shown in Figure 5. The differential stress as a function of axial strain is shown in Figure 5a while the volumetric strain is shown as the function of the mean stress in Figure 5b. Up to 10 MPa of confining pressure, behavior typical of the brittle faulting regime, was observed with stress-strain curves reaching a peak beyond which strain softening was recorded. At confining pressure of 16 MPa and above, a more ductile behavior was observed. At the highest pressure tested (26 and 31 MPa), significant strain-hardening was observed beyond the yield point. WONG *et al.* (1997) showed that the hydrostatic and nonhydrostatic loadings are coupled in a triaxial compression experiment. In the compactive regime, they identified the yield point as the onset of shear-enhanced compaction (CURRAN and CARROLL, 1979), the critical pressure, $C^*$, at which the triaxial volumetric curve manifests an accelerated compaction with respect to a hydrostatic test. They also showed that for porous sandstones this critical pressure corresponds to a dramatic increase in the acoustic emission activity. BAUD *et al.* (2000a) and VAJDOVA *et al.* (2004) determined $C^*$ for a series of experiments on limestone relying on strain gage volumetric data only since they recorded no significant acoustic emission activity during their tests. A similar behavior was observed here: The mean stress-volumetric strain curve was first linear. At $C^*$, compaction accelerated abruptly and significantly. Shear-enhanced compaction was observed in all experiments, even at low confining pressures (Fig. 5b).

### *4.2. Saint-Maximin Limestone*

Seventeen dry and four wet experiments were performed on Saint Maximin limestone. The hydrostatic data for SML are qualitatively similar to those for Majella grainstone (Fig. 6). SML is weaker than Majella grainstone and the onset of grain crushing and pore collapse $P^*$ was equal to 13 MPa in wet conditions. For SML the

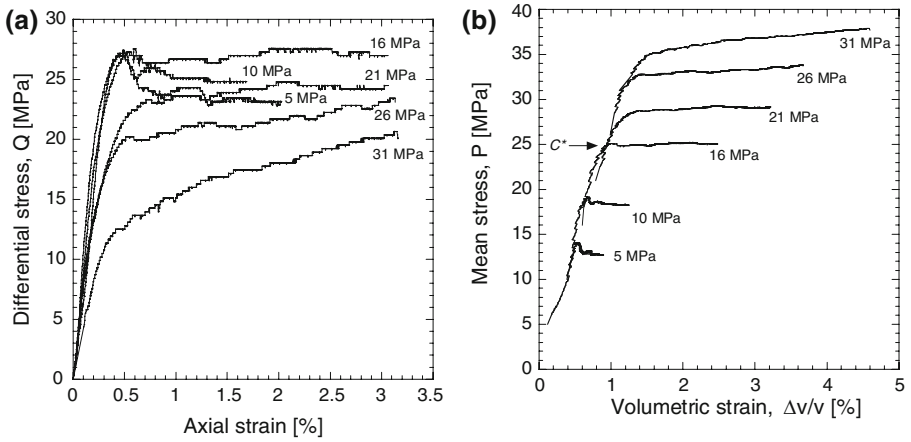


Figure 5
Representative mechanical data for selected triaxial compression experiments on dry Majella grainstone. (a) Differential stress versus axial strain for experiments at confining pressures. (b) Mean stress versus volumetric strain. The mechanical behavior of Majella grainstone is purely compactant.

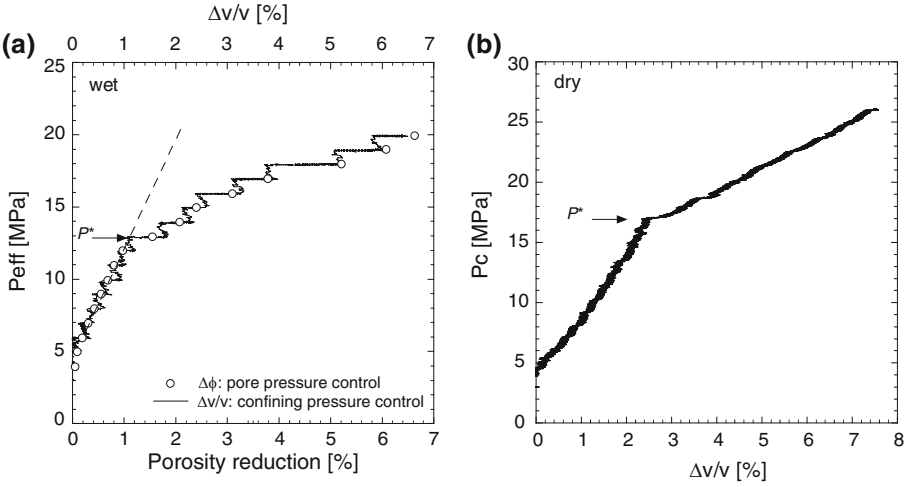


Figure 6
Mechanical data for hydrostatic compression experiments on Saint Maximin limestone. (a) Effective pressure versus porosity reduction (symbols) and volumetric strain (line) for a sample deformed in wet conditions at a constant pore pressure of 10 MPa. (b) Confining pressure versus volumetric strain for a sample deformed in dry conditions. The arrow indicates the critical pressure $P^*$ for the onset of pore collapse.

volumetric strain inferred from the confining pressure monitoring gave results very similar to those inferred from the porosity reduction (Fig. 6a). The volumetric signal for SML represents a proxy for the hydrostat for wet and dry hydrostatic loadings. For

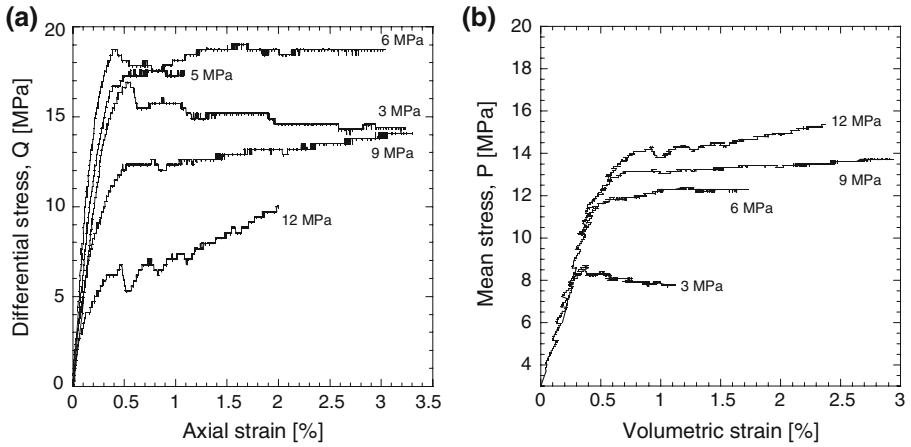


Figure 7
Representative mechanical data for selected triaxial compression experiments on dry Saint Maximin limestone. (a) Differential stress versus axial strain for experiments at confining pressures indicated next to each curve. (b) Mean stress versus volumetric strain. The mechanical behavior of Saint Maximin limestone is purely compactant.

the dry case, the same method as for Majella grainstone was used. The confining pressure was increased at 0.001 MPa/s, giving the onset of grain crushing, $P^*$ equal to 17 MPa.

Triaxial experiments were performed on SML at confining pressures ranging from 3 to 12 MPa. Dissimilar to Majella grainstone, the response of this rock exhibited variability at all pressures. Mechanical data for representative experiments are presented in Figure 7. Three different behaviors were observed: 1) at the lowest confining pressures (3–5 MPa), the stress-strain curves reached a peak beyond which strain softening was observed (Fig. 7a), behavior typical of the brittle faulting regime. Visual inspection of samples indeed revealed the presence of macroscopic failures at relatively high angles with respect to the major principal stress. 2) At confining pressures between 6 and 12 MPa, the stress-strain curves were mostly flat beyond the yield point. In porous sandstone this behavior is typical of a transitional regime (Bésuelle, 2001; Baud *et al.*, 2004) where the failure modes usually involve high angle conjugate shear bands. 3) At the highest confining pressures (12 MPa), the stress-strain curves were punctuated by episodic stress drops while the rock strain hardened. This behavior is comparable to the observations of Baud *et al.* (2004) on Bentheim sandstone in which discrete compaction bands developed. However, in both cases, visual inspection of the samples revealed no clear evidence of strain localization. The failure modes of SML samples were therefore unclear above 5 MPa of confining pressure and a detailed microstructural analysis was performed to describe them (see section 5). Shear-enhanced compaction was observed at all pressure conditions.

Table 2

*Summary of mechanical data for the samples investigated in this study*

| Confining pressure, MPa | Compactive yield stress $C^*$ | | Comments on failure modes |
|---|---|---|---|
| | Differential stress $Q = \sigma_1 - \sigma_3$, MPa | Mean stress $P = (\sigma_1 + 2\sigma_3)/3 - P_p$, MPa | |
| Majella grainstone | | | |
| 5 | 25.5 | 13.5 | compactive shear bands |
| 10 | 24.6 | 18.2 | compactive shear bands |
| 16 | 22.9 | 23.7 | homogeneous cataclastic flow |
| 21 | 19.6 | 27.5 | homogeneous cataclastic flow |
| 26 | 15.7 | 31.3 | homogeneous cataclastic flow |
| 28 | 13.2 | 32.40 | homogeneous cataclastic flow |
| 31 | 10.5 | 34.5 | homogeneous cataclastic flow |
| $P^*$ | | 37 | homogeneous cataclastic flow |
| $P^{*(1)}$ | 0 | 26.5 | homogeneous cataclastic flow |
| Saint Maximin limestone | | | |
| 3 | 8 | 15 | high-angle compactive shear bands |
| 3 | 8.1 | 15.4 | high-angle compactive shear bands |
| 5 | 10. | 14.8 | high-angle compactive shear bands |
| 6 | 10.6 | 13.6 | compactive shear bands |
| 6 | 10.4 | 13.2 | compactive shear bands |
| 9 | 12.8 | 11.5 | compactive shear bands |
| 9 | 12.8 | 11.4 | compactive shear bands |
| 12 | 14.62 | 7.3 | compactive shear bands |
| 12 | 14.1 | 6.2 | compactive shear bands |
| $P^*$ | 0 | 17 | homogeneous cataclastic flow |
| $P^{*(1)}$ | 0 | 13 | homogeneous cataclastic flow |

(1) Wet hydrostatic experiment with $P_p = 10$ MPa

### 4.3. Critical Pressures

The critical pressures $C^*$ for the onset of shear-enhanced compaction are summarized in Table 2. Because no dilatancy was observed in our experiments, for both rocks our data mapped a single failure envelop for $C^*$ for each rock (Fig. 8). For MA, the variability between samples was relatively small and the compactive envelop is well constrained with a few experiments (Fig. 8). For SML we observed some variability between samples and we therefore duplicated all the experiments. Since we measured no significant variations of porosity in our blocks, this variability could be the result of some local variations of the silica content of our samples.

## 5. Microstructural Observations

Selected samples at different stages of deformation were unloaded and retrieved from the pressure vessel. The deformed samples were first impregnated with epoxy and then

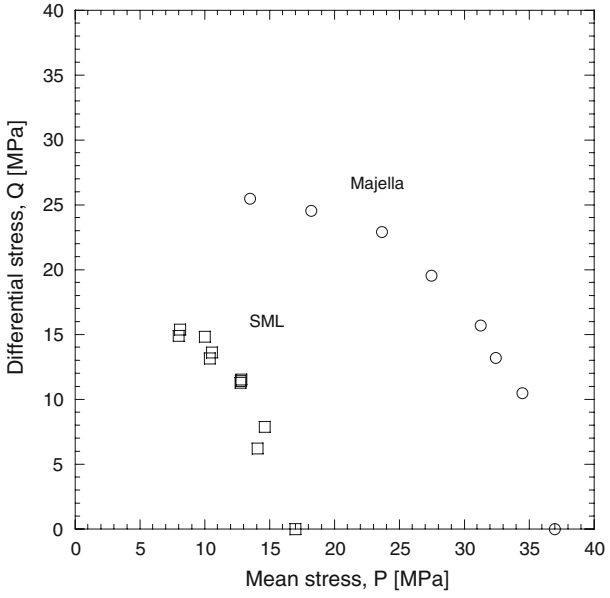


Figure 8
Yield stresses in the stress space *P*-*Q* for: (a) Majella grainstone, (b) Saint Maximin limestone.

sawed along a plane parallel to the axial direction to prepare petrographic thin sections. The thin sections of about 150 μm of thickness were sputter-coated with 0.1 μm of carbon. Back-scattered electron (BSE) images have been taken through a FESEM (see section 2).

### *5.1. Hydrostatic Compaction*

Figure 9 presents a selection of micrographs for two samples of Majella grainstone deformed hydrostatically beyond $P^*$ in dry (Figs. 9a-b) and wet conditions (Fig. 9c). In both wet and dry samples, grain crushing was pervasive. Damage was distributed homogeneously in the samples. The dry sample reached a peak confining pressure of 50 MPa (13 MPa beyond $P^*$) which corresponded to a relatively modest level of plastic strain $< 4\%$. Figure 9a shows that a large proportion of the grains are undamaged and therefore the sample is in an early stage of cataclastic flow. Microcracks appeared to radiate from grain contacts in qualitative agreement with the Hertzian fracture model developed by ZHANG *et al.* (1990). Twinning was observed in a few grains (Fig. 9b) but twinning activity did not appear as an important deformation mechanism at this level of compaction. More intense grain crushing was observed in the wet sample deformed to about 5% of plastic strain, leading to significant grain size reduction (Fig. 9c).

Similar observations were made in samples of SML deformed hydrostatically (Fig. 10). The microstructure of this rock is more complex than Majella grainstone, with

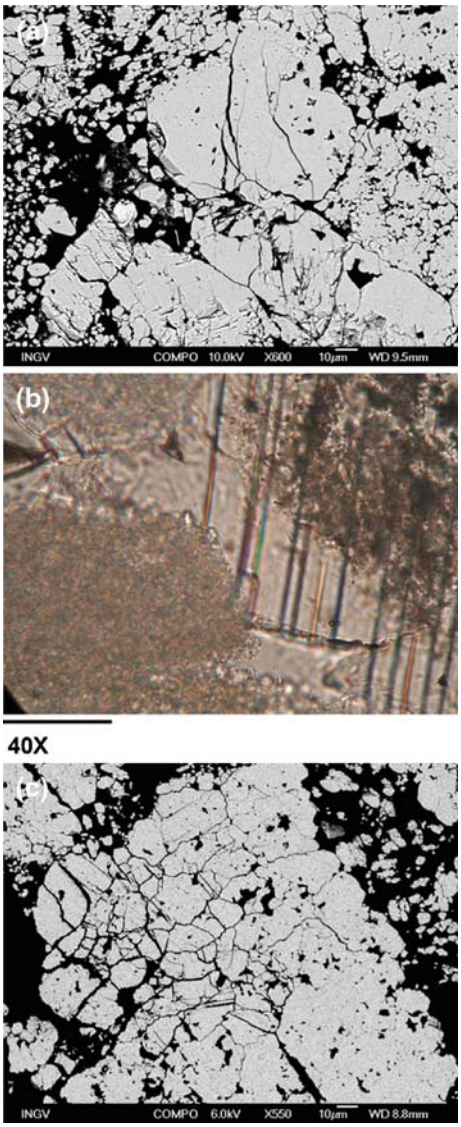


Figure 9
Field emission SEM back-scattered micrographs of Majella grainstone samples deformed hydrostatically beyond $P^*$ in (a) dry and (c) wet conditions. Grain crushing is pervasively observed. Limited twinning activity is visible under transmitted light (b).

calcite and quartz grains and fossils. Figures 10a-c present micrographs of a sample deformed in dry conditions to a confining pressure of 27 MPa (10 MPa beyond $P^*$). Damage appeared homogeneously distributed in this sample and cracking was mostly observed in the quartz and calcite grains and less in the fossils (Figs. 10a-b). Limited

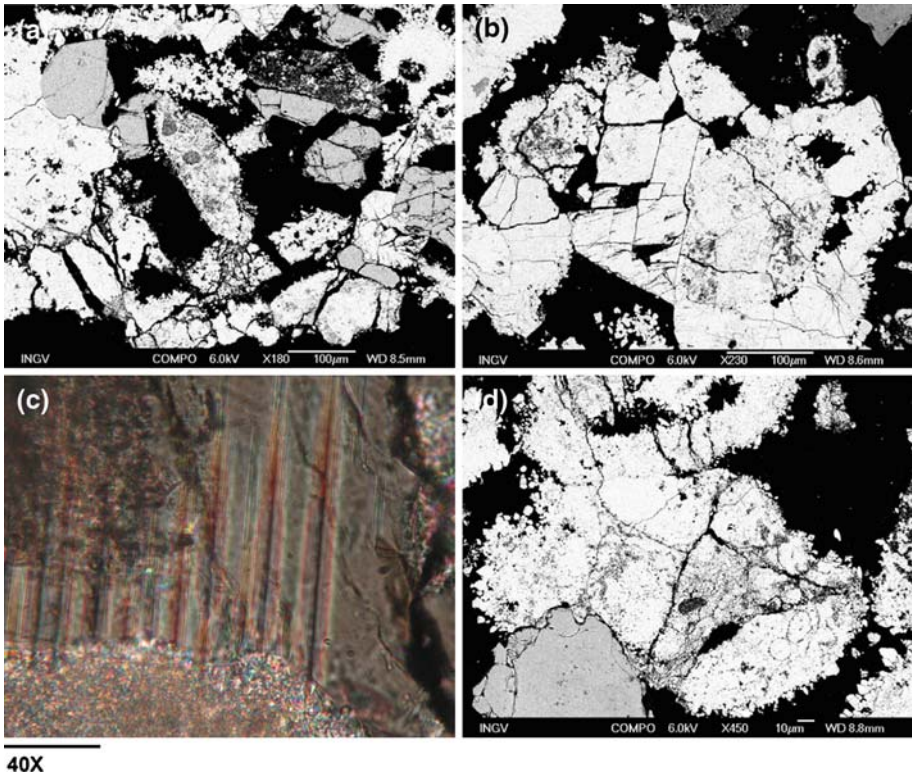


Figure 10
Micrographs of Saint Maximin samples deformed hydrostatically beyond $P^*$ in (a, b, c) dry and (d) wet conditions. Grain crushing is observed in both silicate and carbonate grains. Limited twinning activity is visible under transmitted light (c).

twinning activity was observed in a few calcite grains (Fig. 10c). For a sample deformed in wet conditions to an effective pressure of 20 MPa (7 MPa beyond $P^*$), we observed a similar development of cataclastic flow. The intensity of grain crushing appeared somehow more important in this sample (Fig. 10d). As in Majella grainstone, microcracking initiated from grain contacts and did not appear to differently affect silica and calcite grains. Our observations on both rocks are qualitatively similar to what has been described for porous sandstone of different porosities by Menéndez *et al.* (1996) and Wu *et al.* (2000).

Preliminary measurements revealed an increase of the internal pore surface in hydrostatically deformed samples of Majella grainstone, from 0.15 $m^2/g$ to 0.30 $m^2/g$ for a dry sample pressurized to 50 MPa of confinement. The increase in the pore surface due to microcracking was found directly proportional to the plastic strain and was comparable in dry and wet samples. In SML, no clear increase of the internal pore surface was observed in samples deformed hydrostatically just beyond $P^*$. More intense microcracking (i.e.,

higher plastic strain) was presumably needed to impact significantly the much larger internal pore surface in SML compared to Majella. A systematic study is underway to confirm this first series of observations.

### 5.2. *Shear-Enhanced Compaction*

Mechanical data on dry Majella grainstone (section 4.1) suggest that shear-enhanced compaction is followed by the two main failure modes in this rock: shear failure and cataclastic flow. Microstructural observations performed on a series of triaxially deformed samples confirm these conclusions. At low confining pressure (5–10 MPa), we observed compactive shear bands in all the samples. Figure 11a presents an example for a sample deformed at 5 MPa of confining pressure to an axial strain of 1%. The band has a thickness of about 2 to 3 grains and is oriented at a low angle (45–50°) with respect to the major principal stress. The compactive shear band appears as alternating fine

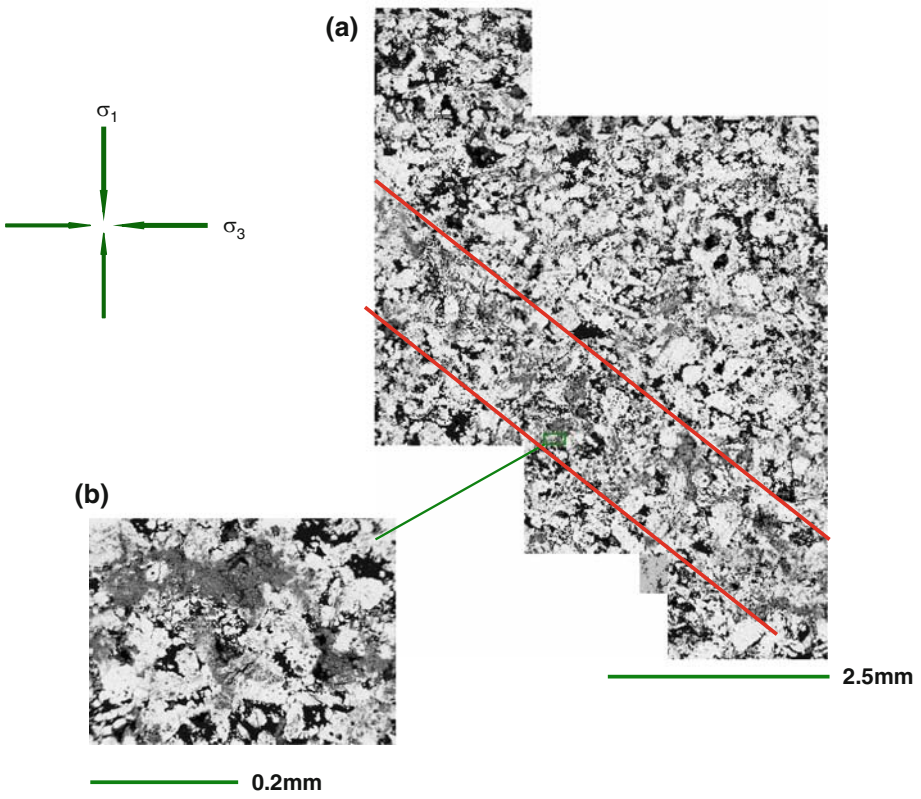


Figure 11
(a) Mosaic of micrographs showing the details of a compactive shear band in a sample of Majella grainstone deformed at 5 MPa of confining pressure. (b) extensive grain crushing inside the band. Maximum principal stress $\sigma_1$ was along the vertical direction.

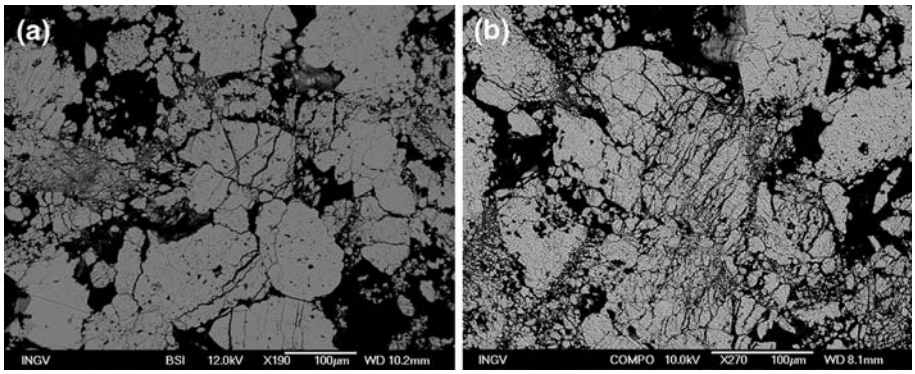


Figure 12
Micrographs of Majella samples deformed in dry conditions at (a) 16 MPa of confining pressure to 3% axial strain; and (b) at 26 MPa confining pressure to 5.8% axial strain. Maximum principal stress $\sigma_1$ was along the vertical direction.

powder layers subparallel to the band orientation and heterogeneously cracked grains (Fig. 11b).

At higher confining pressures (>10 MPa), homogeneous cataclastic flow was observed in all the deformed samples. Figures 12a-b present two typical damaged zones in two samples deformed at 16 MPa of confining pressure and to 3% of axial strain (Fig. 12a) and 26 MPa of confining pressure and 5.8% of axial strain (Fig. 12b). In both cases, the samples were deformed beyond $C^*$ and grain crushing was the dominant deformation mechanism. The level of isotropic damage appeared linked to the amount of plastic strain accumulated in the various studied samples. An example of microcracks initiating from grain contacts is shown in Figure 12a. It corresponds to a plastic volumetric strain of about 1.5% while after an accumulation of 2.3% of plastic volumetric strain some grains are completely crushed, comminuted into micron size particles (Fig. 12b). In some areas, part of the pore space has been filled with fine material. Therefore two distinctly different failure modes were observed in Majella grainstone, i.e., shear failure and cataclastic flow, without any sign of hybrid failure modes, suggesting that the brittle ductile transition occurred over a narrow window of confining pressures in this rock.

The evolution of the failure mode with increasing pressure in Saint-Maximin limestone could not be unambiguously determined from the mechanical data and visual inspections of the samples (section 4.2). Over the confining pressure range of 3 MPa to 12 MPa ($P^*$ is at 17 MPa), various patterns of strain localization were observed in all the samples. At pressures of 3 and 5 MPa, after only a few percent of plastic strain beyond $C^*$, a single band oriented at relatively high angle with respect to the major principal stress was observed. The macroscopic band started in the middle of the sample (Fig. 13) or from one end. In the example presented in Figure 13, the band orientation was about 80 degrees with respect to the major principal stress. The band has a thickness of 3 to 4

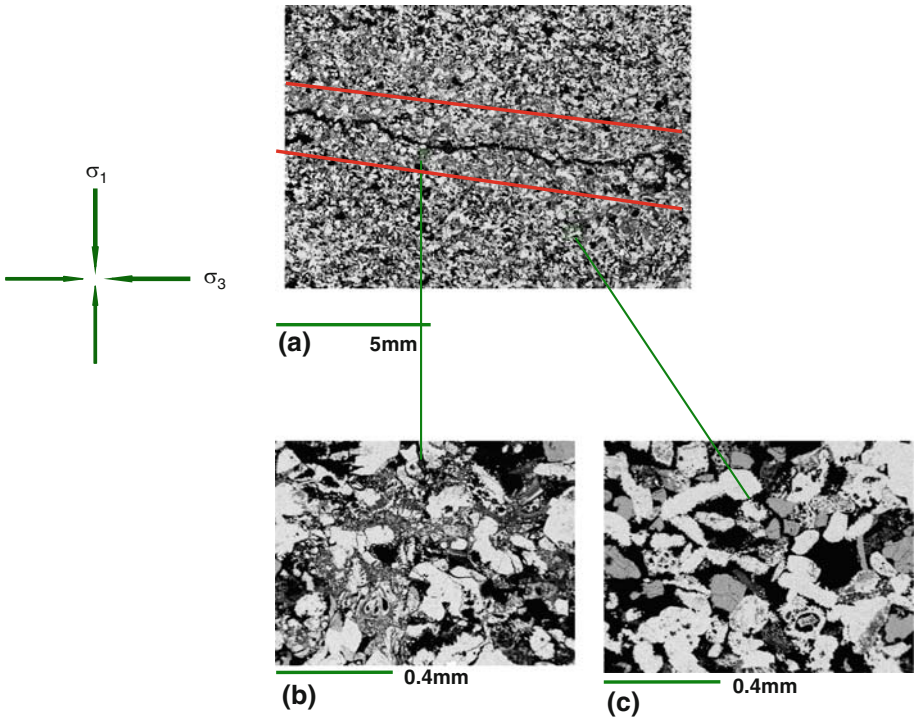


Figure 13
(a) Mosaic of micrographs showing the details of a high angle compactive shear band in a sample of Saint Maximin limestone deformed in dry conditions at 5 MPa of confining pressure. Details of (b) intense grain crushing inside the band and (c) the absence of damage outside the band. Maximum principal stress $\sigma_1$ was along the vertical direction.

grains and no significant damage was visible outside the band. A macroscopic crack developed in the central part of the band, suggesting that this structure is not purely compactant and therefore is interpreted as a compactive shear band. At higher confining pressures (9, 10 and 12 MPa), more complex and very variable spatial distribution of damage is observed. Damage appeared in all cases in a few compactive shear bands (from 2 to 4) oriented at various orientations with respect to the major principal stress. Figure 14 shows two examples for samples deformed at 9 MPa (Fig. 14a) and 10 MPa (Fig. 14b) of confining pressure. The compactive shear bands appear as dark bands if the sample is saturated with colored epoxy. Inside the bands, intense grain crushing was observed (Fig. 14d) while no visible damage appeared outside (Fig. 14c). Since for the same pressure conditions significantly different microstructures were observed in different samples, it is likely that pre-existing heterogeneities in the samples played a role in the nucleation and development of the compactive shear bands. Differing from Majella limestone, compaction localization was the dominant feature of compaction in triaxially deformed SML samples.

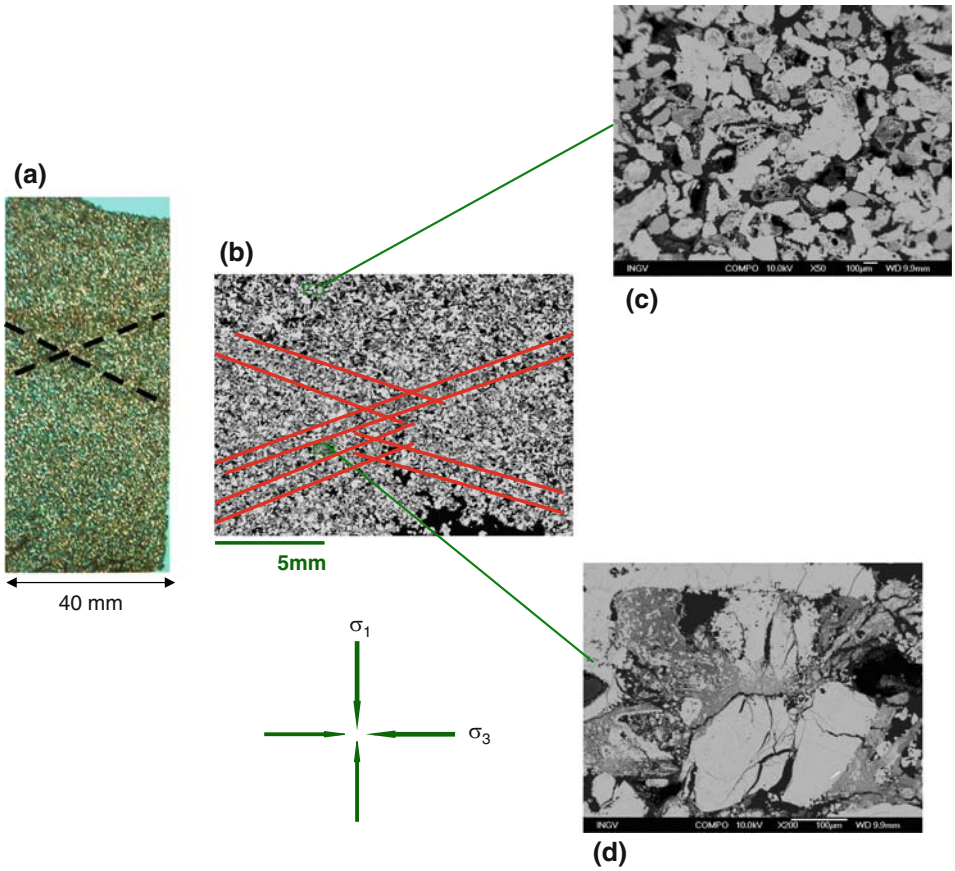


Figure 14
Optical (a) and Field Emission SEM micrographs mosaic (b) of compactive shear bands in samples of Saint Maximin limestone deformed in dry conditions at 9 and 10 MPa of confining pressure, respectively. Details showing (c) no damage outside the band; (d) intense grain crushing inside the band. Maximum principal stress $\sigma_1$ was along the vertical direction.

## 6. Discussion

### 6.1. Microstructural Control of Strength in Porous Carbonates

Microstructural observations indicate that microcracking was the dominant mechanism of deformation in both Majella grainstone and SML at both hydrostatic and triaxial conditions. In hydrostatically deformed samples, extensive cracking occurred mostly from grain contacts in qualitative agreement with the Hertzian fracture model developed by ZHANG *et al.* (1990). This model was based on observations on sandstones and predicts that for a rock of porosity $\phi$ and grain radius $R$, the critical pressure $P^*$ follows the trend $P* \propto (\phi R)^{-3/2}$. VAJDOVA *et al.* (2004) compiled published values of $P^*$ for carbonates and siliciclastic rocks and compared them with this model. For the same value of $\phi R$, they showed that the

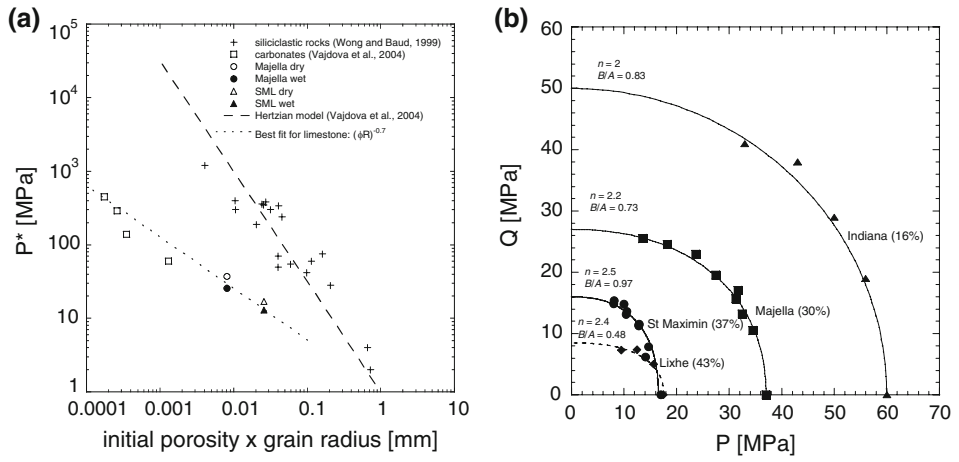


Figure 15

(a) Critical pressure $P^*$ for the onset of grain crushing in various carbonates under hydrostatic loading as a function of the product of initial porosity and grain radius. Open symbols represent data for dry conditions and dark symbols represent data for wet conditions, for Solnhofen limestone (Baud *et al.*, 2000a), Tavel limestone, Indiana limestone (Vajdova *et al.*, 2004), Chauvigny limestone (Fabre and Gustkiewicz, 1997), Majella grainstone and Saint Maximin limestone (this study). The crosses represent data for siliciclastic rocks from Wong and Baud (1999). The dashed line is a prediction of the Hertzian fracture model. The dotted line is the best fit for the carbonate rocks. (b) Compilation of yield envelopes for carbonate rocks. Initial porosity is indicated for each rock. Data sources: Lixhe chalk: Homand and Shao (2000), Indiana limestone: Vajdova *et al.* (2004), Majella grainstone and Saint Maximin limestone: this study. The curves represent the best fit using the model of Grueschow and Rudnicki (2005).

limestones are significantly weaker than the siliciclastic rocks and that they do not follow the trend predicted by the Hertzian model. In Figure 15a, we added the critical pressure $P^*$ for Majella and SML in dry and wet conditions to Vajdova *et al.* (2004) compilation. Our new data confirmed their conclusions and the whole set of limestone data follows a much less steep trend $P^* \propto (\phi R)^{-0.7}$. Because crystal plasticity did not appear to be a major factor leading to the observed pore collapse in our samples, the discrepancy between the Hertzian model and the measured $P^*$ for carbonates reflects an intrinsic limit of the model in particular because it considers uniform defect structure (Vajdova *et al.*, 2004). The results shown here indicate that more data, particularly for weaker materials, will be needed to confirm this trend, and more elaborate models should be developed. Baud *et al.* (2000b) analyzed the effect of water in conventional triaxial experiments on porous sandstone. They interpreted the water-weakening effect as due to the reduction of the surface energy in the presence of water and quantified this effect using a parameter $\lambda$ defined as:

$$\lambda = \left(\frac{\gamma'}{\gamma}\right) = \left(\frac{P^*_{\text{wet}}}{P^*_{\text{dry}}}\right)^{2/3},$$

where $\gamma$ and $\gamma'$ are the surface energies in dry and wet conditions, respectively. From our hydrostatic dry and wet data, we inferred $\lambda = 0.80$ and $\lambda = 0.84$ for Majella grainstone

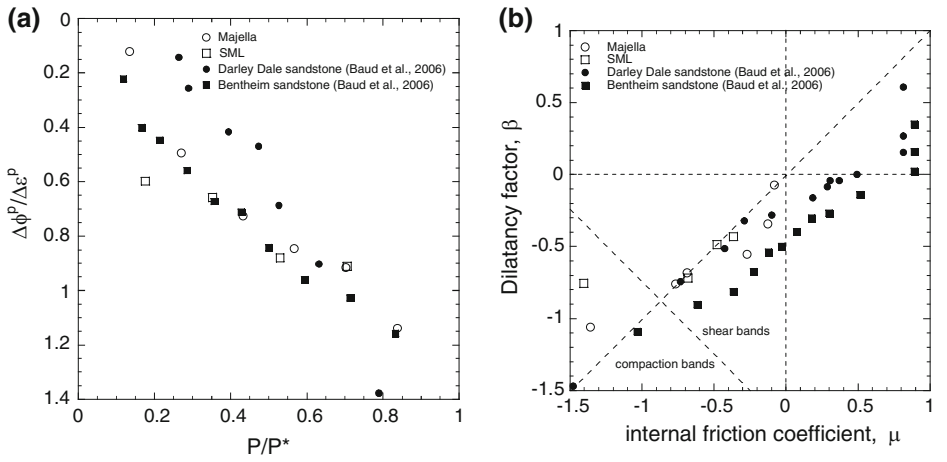


Figure 16

(a) Compaction factor at the onset of shear-enhanced compaction $C^*$. Open symbols represent data for Majella grainstone and Saint Maximin limestone (this study), dark symbols represent data for Bentheim and Darley Dale sandstone (Baud *et al.*, 2006). (b) Constitutive parameters for the nonassociative model of Rudnicki and Rice (1975). The dilatancy factor $\beta$ is plotted as a function of the internal friction coefficient $\mu$. The open symbols represent the data for Majella grainstone and Saint Maximin limestone (this study). For reference data for samples of Bentheim and Darley Dale sandstone (Baud *et al.*, 2006) are given as dark symbols. Two of the failure modes (compaction bands and shear bands) predicted from bifurcation analysis (Issen and Rudnicki, 2000) are separated by the dashed line $\beta + \mu = -\sqrt{3}$. The normality line $\beta = \mu$ is also represented as a dashed line.

and SML, respectively. Baud *et al.* (2000b) found values in the range [0.79; 0.97] with the lower value for Boise sandstone in the same porosity range as Majella and SML. This suggests that the weakening effect of water measured in our carbonates can also be due to the reduction of the surface energy. Previous studies reported a weakening effect of water of various magnitudes in carbonates (Boozer *et al.*, 1963; Rutter, 1974; Risnes *et al.*, 2005). Several chemical mechanisms, in particular pressure solution (Hellmann *et al.*, 1996) and stress corrosion (Hadizadeh and Law, 1991) were proposed to explain the observed reduction in strength. Pressure solution was unlikely to be a factor in our experiments performed at room temperature over short periods of time. The stress corrosion effect leads to macroscopic creep and time-dependent behavior both in extension and in compression (Atkinson and Meredith, 1987; Baud and Meredith, 1997). Our wet experiments were performed under fully servo-controlled pore fluid pressure and no significant macroscopic creep was observed. It suggests that stress corrosion only slightly impacted on our results, if any. Risnes and Flaageng (1999) and Heggheim *et al.* (2005) studied the weakening effect of pore fluid on chalks. They showed that the strength of chalks is strongly dependent on the nature of the pore fluid and increases according to: water < methanol < oil < dry. Risnes *et al.* (2005) performed a systematic study on Lixhe chalk of porosity > 40% using water-glycol mixtures. Their data for water saturated and glycol saturated cases would lead to $\lambda < 0.60$ for Lixhe

chalk. However, Risnes *et al*. (2005) interpreted part of this very important weakening as the result of complex capillary effects (since dry chalk still contains water). Because the strength reduction observed in our wet samples was much less pronounced and comparable for two rocks of very different internal surfaces, it is unlikely that such capillary effects contributed significantly to the water weakening in Majella grainstone and SML.

In Figure 15b we compile our data in the stress space ($P-Q$) and compare them with Vajdova *et al*.'s (2004) data on Indiana limestone of 16% porosity and data on Lixhe chalk of 43% porosity from Homand and Shao (2000). Figure 15b shows clearly that porosity significantly influences the strength of porous carbonates. Unlike for porous sandstone for which the compactive failure envelopes can in most cases be fitted with an elliptical cap (Wong *et al*., 1997; Baud *et al*., 2006), the failure envelopes of porous carbonates display a wide variety of shapes. To quantify the differences in the shapes, we used an expression proposed by Grueschow and Rudnicki (2005):

$$\left(\frac{P}{A}\right)^n + \left(\frac{Q}{B}\right)^n = 1. \tag{1}$$

The exponent $n$ varies from 2 to 2.5 and seems to increase with increasing porosity. The ratio $B/A$ also shows a wide variability from 0.48 to 0.97. This variability underlines the difficulty of the constitutive modeling of porous carbonates. Attempts using a model based on plastic pore collapse (Curran and Carroll, 1979; Baud *et al*., 2000a; Vajdova *et al*., 2004) yielded in most cases limited success. Vajdova *et al*. (2004) suggested that a more appropriate model should consider the coupling of plasticity and microcracking. Such an approach is however unlikely to apply to our new data, considering the lack of evidence of crystal plasticity in deformed samples of Majella grainstone and SML. A more appropriate micromechanical model should take into account the geometric complexity of the rock microstructure (pore shape, grain size distribution, etc). It would therefore require more mechanical data, and particularly a very accurate description of the rock microstructure employing techniques such as mercury porosimetry, BET and further quantitative microstructural analyses using various techniques of imaging such as Computed Tomography (CT). Building such a model is beyond the scope of this study, however mechanical and microstructural data presented here could be adopted as a referring base.

### 6.2. *Compaction Localization in Porous Carbonates*

Several studies have described experimentally the brittle-ductile transition in sandstone (Wong *et al*., 1997; Bésuelle, 2001; Baud *et al*., 2004) and carbonates (Paterson, 1958; Heard, 1960; Evans *et al*., 1990; Vajdova *et al*., 2004). In porous sandstone, recent experimental work revealed a wide variety of failure modes involving compaction localization at effective pressure higher than that of brittle failure. With

increasing effective pressure, a transition from dilatancy to compaction is observed while the failure evolves from dilating shear-band to high angle compactive shear bands mostly on the left-hand side of the failure envelope. Further increase in the effective pressure leads to the developments of homogeneous cataclastic flow or in many cases to the sequential growth of discrete compaction bands (Baud *et al.*, 2004; 2006). The brittle-ductile transition in sandstone is therefore not a sharp transition and not concomitant to the dilatant/compactant transition. In rocks where the pervasive development of compaction bands is observed, the terminology brittle-ductile transition is actually not really suitable since ductile deformation occurred mostly under hydrostatic conditions. In porous limestone, the data of Vajdova *et al.* (2004; 2006) suggest that the transition between the dilatant brittle regime and homogeneous catatclastic flow is sharper and relatively closer to the dilatant/compactant transition. However, more microstructural data are needed to confirm this tendency.

The behavior of Majella and SML is different from that of less porous limestones, in particular because of the absence of dilatancy. Compactive shear bands were observed at the lowest tested pressures in both rocks. Unlike for sandstone, we had no evidence of the band angle decreasing with increasing pressure. A quantitative description of the band geometries (orientation, tortuosity, thickness) would be very difficult to give because of the variability between samples and the small interval of pressures at which the bands were observed to form for these weak materials. In Majella limestone this failure mode is followed by homogeneous cataclastic flow, and the compactive behavior of this rock at high pressures appears similar to that of Indiana and Tavel limestones (Vajdova *et al.*, 2004). The Majella limestone used in this study was from the host rock in the S. Madonna delle Mazze quarry described by Tondi *et al.* (2006). A variety of structures involving deformation and compaction bands and stylolites was observed in the quarry. The deformation bands are oriented at various angles to the bedding and show both porosity reduction and shearing. In this sense, they are comparable to the compactive shear bands observed at low confinement in the laboratory experiments. The compaction bands were the first structures of this type observed in a carbonate rock (Tondi *et al.*, 2006). These field compaction bands are mostly oriented parallel to the bedding direction. Recent experiments on porous sandstones (Townend *et al.*, 2008; Louis *et al.*, 2009, this volume) indeed support the idea that in a material with significant bedding anisotropy, compaction bands tend to develop preferentially in the bedding plane. Starting from a comparable host material taken from the same formation, we observed no evidence of compaction bands in our laboratory samples, although they were cored in the most favorable orientation (i.e., perpendicular to bedding). This suggests that the field compaction bands could have appeared after the deformation bands and were the results of complex stress interactions between different structures. It is also possible that water played a major role in the evolution of the failure in this type of material. Wet triaxial experiments are currently being performed in our laboratory to study this question.

Compaction localization appeared in all triaxially deformed samples of Saint Maximin limestone and can be considered for this carbonate as the dominant feature of

compaction. However, a certain number of differences were observed with respect to the patterns of compaction localization reported in porous sandstones. First, when the deformation is localized, the bands observed in SML were in most cases not orthogonal to the major principal stress and thus not labeled as compaction bands. Second, bands appeared less tortuous and thicker than the discrete compaction bands observed in Bentheim and Diemelstadt sandstones (Baud *et al*., 2004). The sequential growth of the bands, similarly to the sandstone, seemed strongly influenced by the presence of heterogeneities in the sample. Given the weak velocity anisotropy measured in this rock (see section 2), it is unlikely that the sample orientation with respect to the sedimentary bedding played a key role in our observations. Further analysis is needed to understand the nucleation and growth of these bands. Some variability in the quartz content and spatial distribution of quartz grains in the samples could explain the relative scattering observed in the mechanical data, as well as the variability in the failure modes. Dresen *et al*. (1998) showed that a synthetic marble containing about 20% quartz is about 5 times stronger than without quartz. The relative weakness of SML and the fact that $P^*$ follows the carbonate trend (Fig. 15a) suggest some complex quartz-calcite interaction in this rock. It will be difficult to improve our understanding of these hard/soft grain interactions and their impact on strain localization relying solely on more microstructural work. Recent studies using X-ray computed tomography (Louis *et al*., 2006, 2007) showed that it is possible to image anisotropic damage in a nondestructive way. This technique could be used on SML to characterize the heterogeneity of this material and facilitate understanding of the onset of compaction localization. The pilot use of Digital image correlation on CT images of intact and deformed samples gave promising results on sandstone (Louis *et al*., 2007). It will be the subject of future work on SML.

In a recent study, Baud *et al*. (2006) determined the constitutive parameters for a series of porous sandstones and checked the prediction of bifurcation analysis (Rudnicki and Rice, 1975; Issen and Rudnicki, 2000) focusing on compaction localization. Because we observed compaction localization in both studied carbonates, we quantified as a pilot study the constitutive parameters for both Majella and SML. Following Wong *et al*. (1997) we inferred the plastic compaction factor from:

$$\frac{\Delta\varepsilon_{kk}^{p}}{\Delta\varepsilon_{1}^{p}} = \frac{(\Delta\varepsilon_{kk}/\Delta\varepsilon_{1}) - \phi\beta_{\phi}[\Delta Q/\Delta\varepsilon_{1}]}{1 - [\Delta Q/\Delta\varepsilon_{1}]/E}, \tag{2}$$

where $\beta_\phi$ is the pore compressibility, $\varepsilon_1$ the axial strain and $E$ Young's modulus.

In Figure 16a, the plastic compaction factor is presented as a function of the effective pressure normalized by $P^*$. The data of Baud *et al*. (2006) for Darley Dale and Bentheim sandstone are given for reference. Since only compaction was observed in the experiments reported here, the plastic compaction factor for the dry experiments is positive. The evolution with pressure is very similar the one observed in the more porous Bentheim sandstone ($\phi = 23\%$). Darley Dale sandstone behaves somewhat differently,

most probably because of its lower porosity (13%). Most of our measurements fall in the range $0 < \Delta\varepsilon_{kk}^p/\Delta\varepsilon_1^p < 1$, with the implication that $0 < \Delta\varepsilon_{kk}^p < \Delta\varepsilon_1^p$. Since $d\varepsilon_{kk}^p = d\varepsilon_1^p + 2d\varepsilon_3^p$ in a conventional triaxial experiment, our data require that inelastic yield in these carbonates be accompanied by an overall reduction in volume that involves the interplay of axial shortening ($d\varepsilon_1^p > 0$ with our sign convention) and lateral expansion $\left(d\varepsilon_2^p = d\varepsilon_3^p < 0\right)$.

Conditions for strain localization in the context of the bifurcation analysis were formulated by RUDNICKI and RICE (1975) for shear localization and more recently by ISSEN and RUDNICKI (2000) for compaction localization. In this framework, these conditions were expressed in terms of a dilatancy factor $\beta$ and a friction parameter $\mu$ defined for a conventional triaxial experiment as:

$$\beta = -\sqrt{3}\,\frac{\Delta\varepsilon_{kk}^p/\Delta\varepsilon_1^p}{\left(3 - \Delta\varepsilon_{kk}^p/\Delta\varepsilon_1^p\right)} \quad \text{and} \quad \mu = \frac{1}{\sqrt{3}}\frac{\partial Q}{\partial P}, \text{respectively.}$$

In particular, ISSEN and RUDNICKI (2000) showed that compaction bands should develop if:

$$\mu + \beta < -\sqrt{3}. \tag{3}$$

Figure 16b illustrates that overall our new data on carbonates are relatively close to the normality line $\beta = \mu$. For a comparable value of $\mu$, the compaction factor is significantly lower than the estimations for Bentheim sandstone in which discrete compaction bands were observed. A majority of the points for Majella grainstone and Saint Maximin limestone falls in the domain where shear bands are predicted, in agreement with our microstructural observations. WONG *et al.* (2001) showed that in this parameter range, the theory also predicts strain-softening. Although we did not calculate the hardening parameter, because both strain-softening and strain-hardening were observed in the mechanical data (Figs. 5 and 7), some discrepancies exist between our observations on carbonates and the theoretical predictions. WONG *et al.* (2001) observed more significant discrepancies in sandstone, for which the theory failed to predict the apparition of compaction bands. They attributed the observed discrepancies to the inadequacy of the constitutive model to capture the partitioning of several mechanisms, such as stress-induced microcracks, pore collapse and grain crushing. Similar conclusions may be applicable here. Work is ongoing to collect more data to confirm these preliminary results, particularly tests performed under wet conditions, within which the dilatancy factor $\beta$ is better constrained.

## 7. Conclusion

We presented recent advances of a work in progress on two very porous carbonates, Majella grainstone and Saint Maximin limestone. New data indicate that the mechanical

behavior of porous carbonates is dominated by shear-enhanced compaction associated, in most cases, with strain-hardening. Stress-induced cracking and grain crushing are the dominant micromechanisms of deformation in both rocks, with no major crystal plasticity being observed. In Majella limestone, compactive shear bands comparable to the field deformation bands were observed at low confinement. At higher pressures, compaction localization was inhibited and homogeneous cataclastic flow developed. Recent field observations suggested the development of compaction bands in the Majella formation. Further laboratory and microstructural work will be needed to explain the discrepancies between the failure mode observed in the laboratory and the structures described in the field. In the more porous Saint-Maximin limestone, compaction localization was observed in all of the triaxially deformed samples. Localized bands developed at various orientations with respect to major principal stress. These bands are interpreted as compactive shear bands. The number of bands increases with increasing strain. Although compaction localization can develop in porous carbonates, it remains unclear whether discrete compaction bands can develop in such materials. Identifying compaction localization in porous carbonates has proven more difficult than for porous sandstones, mostly because the carbonates are essentially made of calcite. To further understand the development of the localized deformation structures in porous carbonates, microstructural analyses are being combined with X-ray computed tomography to capture the 3D geometry of the bands and to better understand their formation.

## *Acknowledgments*

We are grateful to Emanuele Tondi who kindly furnished us with a block of Majella grainstone. In Strasbourg, we benefited from the very valuable technical assistance of Jean-Daniel Bernard. In Cergy-Pontoise, part of the measurements were done by Jean-Christian Colombier, Matthieu Angeli, Lisa Casteleyn and Romain Giros. We thank Silvio Mollo for assisting with the grain size analysis. We also benefited from discussions with Teng-fong Wong, Veronika Vajdova, and Laurent Louis. We are grateful to Dave Olgaard and Alexandre Schubnel for thoughtful reviews. This research was partially supported by the CNRS/CNR bilateral agreement (Project 19138). SV was supported from FIRB-MIUR Project "Research and Development of New Technologies for Protection and Defense of Territory from Natural Risks".

## References

Angeli, M., Benavente, D., Bigas, J.-P., Menéndez, B., Hébert, R., and David, C. (2008), *Modification of the porous network by salt crystallization in experimentally weathered sedimentary stones*, Mater. Struct., *41*, 1091–1108.

Atkinson, B.K. and Meredith, P.G. *The theory of subcritical crack growth with applications to minerals and rocks*. In (ed. B.K. Atkinson) *Fracture Mechanics of Rocks*, pp. 111–166, (Academic Press, London. 1987).

BAUD, P. and MEREDITH, P.G. (1997), *Damage accumulation during triaxial creep of Darley Dale sandstone from pore volumometry and acoustic emission*, Int. J. Rock Mech. Min., *34*, 3–4.

BAUD, P., SCHUBNEL, A., and WONG, T.-F. (2000a), *Dilatancy, compaction and failure mode in Solnhofen limestone*, J. Geophys. Res. *195*, 19289–19303.

BAUD, P., ZHU, W., and WONG, T.-F. (2000b), *Failure mode and weakening effect of water on sandstone*, J. Geophys. Res. *105*, 16371–16389.

BAUD, P., KLEIN, E., and WONG, T.-F. (2004), *Compaction localization in porous sandstones: Spatial evolution of damage and acoustic emission activity*, J. Struct. Geol. *26*, 603–624.

BAUD, P., LOUIS, L., DAVID, C., RAWLING, G.C., and WONG, T.-F. (2005), *Effects of bedding and foliation on mechanical anisotropy, damage evolution and failure mode*. In (eds Bruhn, D. and Burlini, L.) *High-Strain Zones: Structure and Physical Properties*. Geological Society of London Special Publications *245*, 223–249.

BAUD, P., VAJDOVA, V., and WONG, T.-F. (2006), *Shear-enhanced compaction and strain localization: Inelastic deformation and constitutive modeling of four porous sandstones*, J. Geophys. Res. *111* (B12401), doi: 10.1029/2005JB004101.

BÉSUELLE, P. (2001), *Compacting and dilating shear bands in porous rocks: Theoretical and experimental conditions*, J. Geophys. Res. *106*, 16371–16389.

BOOZER, G.D., HILLER, K.H., and SERDENGECTI, S. (1963), *Effect of pore fluids on the deformation behavior of rocks subjected to triaxial compression*, 5th Symp. on Rock Mechanics, Univ. Minnesota, 1962, 579–625.

BRACE, W.F. (1978), *Volume change during fracture and frictional sliding: A review*, Pure Appl. Geophys. *116*, 603–614.

BRUNAUR, S., EMMET, P.H., and TELLER, E. (1938), *Adsorption of gasses in multimolecular layers*, J. Amer. Chem. Soc. *60*, 309.

CURRAN, J.H. and CARROLL, M.M. (1979), *Shear stress enhancement of void compaction*, J. Geophys. Res. *84*, 1105–1112.

DAVID, C., ROBION, P., and MENÉNDEZ, B. (2007), *Anisotropy of elastic, magnetic, and microstructural properties of the Callovo-Oxfordian argillite*, Phys. Chem. Earth *32*, 145–153.

DRESEN, G., EVANS, B., and OLGAARD D.L. (1998), *Effect of quartz inclusions on plastic flow in marble*, Geophys. Res. Lett. *25*, 1245–1248.

EDMOND, J.M. and PATERSON, M.S. (1972), *Volume change during the deformation of rocks at high pressures*, Int. Rock Mech. Min. Sci. *9*, 161–182.

EVANS, B., FREDRICH, J.T., and WONG, T.-F. (1990), The brittle-ductile transition in rocks: Recent theoretical and experimental progress. In (eds. A.G. Duba, W.B. Durham, J.W. Handin, H.F. Wang), *The Brittle-Ductile Transition in Rocks (The Heard Volume)*, Geophys. Monogr. Vol. *56*, pp. 1–20.

FABRE, D. and GUSTKIEWICZ, J. (1997), *Poroelastic properties of limestones and sandstones under hydrostatic conditions*, Int. J. Rock Mech. Min. Sci. *34*, 127–134.

FORTIN, J., SCHUBNEL, A., and GUÉGUEN, Y. (2005), *Elastic wave velocities and permeability evolution during compaction of Bleurwiller sandstone*, Int. Rock Mech. Sci. *42*(7–8), 873–889.

FORTIN, J., STANCHITS, S., DRESEN, G., and GUÉGUEN, Y. (2006), *Acoustic Emission and velocities associated with the formation of compaction bands in sandstone*, J. Geophys. Res. *111*, B10203, doi:10.1029/2005JB003854.

FREDRICH, J.T., EVANS, B., and WONG, T.-F. (1989), *Micromechanics of the brittle to plastic transition in Carrara marble*, J. Geophys. Res. *95*, 10,907–10,920.

GRUESCHOW, E. and RUDNICKI, J.W. (2005), *Elliptical yield cap constitutive modeling for high porosity sandstone,* Int. J. Solids Struct. *42*, 4574–4587.

HADIZADEH, J. and LAW, R.D. (1991), *Water-weakening in quartzite deformed at various stress and strain rates,* Int. J. Rock. Mech. Min. Sci. Geomech. Abstr. *28*(5), 431–439.

HADIZADEH, J. and RUTTER, E.H. (1983), *The low temperature brittle-ductile transition in a quartzite and the occurrence of cataclastic flow in nature*, Geol. Rundsch. *72*, 493–509.

HANDIN, J. and HAGER, R.V. (1957), *Experimental deformation of sedimentary rocks under confining pressure: Tests at room temperature on dry sample*, Am. Assoc. Pet. Geol. Bull. *41*, 1–50.

HEARD, H.C. (1960), *Transition from brittle fracture to ductile flow in Solnhofen limestone as a function of temperature, confining pressure and interstitial fluid pressure*. In (eds. D.T. Griggs and J. Handin) *Rock Deformation*, Mem. Geol. Soc. Am. *79*, 193–226.

HEGGHEIM, T., MADLAND, M.V., RISNES, R., and AUSTAD, T. (2005), *A chemical-induced enhanced weakening of chalk by seawater*, J. Petrol. Sci. Eng. *46*, 171–184.

HELLMANN, R., GRATIER, J.P., and RENDERS, P. (1996), *Deformation of Chalk by pressure solution*, V.M. Goldschmidt Conf., Heidelberg.

HOMAND, S. and SHAO, J.F. (2000), *Mechanical behaviour of a porous chalk and effect of saturating fluid*, Mech. Cohes.-Frict. Mater. *5*, 583–606.

ISSEN, K.A. and RUDNICKI, J.W. (2000), *Conditions for compaction bands in porous rock*, J. Geophys. Res. *105*, 21529–21536.

KLEIN, E. and REUSCHLÉ, T. (2004), *A pore crack model for the mechanical behaviour of porous granular rocks in the brittle deformation regime*, Int. J. Rock Mech. Min. Sci. *41*, 975–986.

LOUIS, L., ROBION, P., and DAVID, C. (2004), *A single method for the inversion of anisotropic data sets with application to structural studies*, J. Struct. Geol. *26*, 2065–2072.

LOUIS, L., DAVID, C., METZ, V., ROBION, P., MENÉNDEZ, B., and KISSEL, C. (2005), *Microstructural control on the anisotropy and transport properties in undeformed sandstones*, Int. J. Rock Mech., *42*/7-8, 911–923.

LOUIS, L., WONG, T.-F., BAUD, P., and TEMBE, S. (2006), *Imaging strain localization by X-ray computed tomography: Discrete compaction bands in Diemelstadt sandstone*, J. Struct. Geol. *28*, 762–775.

LOUIS, L., WONG, T.-F., and BAUD, P. (2007), *Imaging strain localization by X-ray radiography and digital image correlation: Deformation bands in Rothbach sandstone*, J. Struct. Geol. *29*, 129–140.

LOUIS, L., BAUD, P., and WONG, T.-F. (2009) *Microstructural inhomogeneity and mechanical anisotropy associated with bedding in Rothbach sandstone*, Pure Applied Geophysics *166*, 517.

MENÉNDEZ, B., ZHU, W., and WONG, T.-F. (1996), *Micromechanics of brittle faulting and cataclastic flow in Berea sandstone*, J. Struct. Geol. *18*, 1–16.

PATERSON, M.S. (1958), *Experimental deformation and faulting in Wombeyan marble*, Geol. Soc. Am. Bull. *69*, 465–476.

RISNES, R. and FLAAGENG, O. (1999), *Mechanical properties of chalk with emphasis on chalk-fluid interactions and micromechanical aspects*, Oil and Gas Sci. Tech., *54*, 6, 751–758.

RISNES, R., MADLAND, M.V., HOLE, M., and KWABIAH, N.K. (2005), *Water weakening of chalk – Mechanical effects of water-glycol mixtures*, J. Petrol. Sci. Eng. *48*, 21–36.

ROBERTSON, E.C. (1955), *Experimental study of the strength of rocks,* Bull. Geol. Soc. Am. *66*, 1275–1314.

RUDNICKI, J.W. and RICE, J.R. (1975), *Conditions for the localization of deformation in pressure sensitive dilatant materials*, J. Mech. Phys. Sol. *23*, 371–394.

RUTTER, E.H. (1974), *The influence of temperature, strain rate and interstitial water in the experimental deformation of calcite rocks*, Tectonophysics *22*, 311–334.

RUTTER, E.H. and MAINPRICE, D.H. (1978), *The effect of water on stress relaxation on faulted and unfaulted sandstone*, Pure Appl. Geophys. 116, 634–654.

TEMBE, S., BAUD P., and T.-F. WONG (2008), *Stress conditions for the propagation of discrete compaction bands in porous sandstone*, J. Geophys. Res., *113*, B09409, doi:10.1029/2007JB005439.

TEUFEL, L.W., RHETT, D.H., and FARRELL, H.E. (1991), *Effect of reservoir depletion and pore pressure drawdown on in situ stress and deformation in the Ekofisk field*, North Sea, Proc. U.S. Rock Mech. Symp. *32*, 63–72.

TONDI, E., ANTONELLINI, M., AYDIN, A., MARCHEGIANI, L., and CELLO G. (2006), *The role of deformation bands, stylolites in fault development in carbonate grainstones of Majella mountain, Italy*, J. Struct. Geol. *28*, 376–391.

TOWNEND, E., BAUD, P., and MEREDITH, P.G. (submitted), *Permeability anisotropy during triaxial deformation of Diemelstadt sandstone*, J. Geophys. Res.

VAJDOVA, V., BAUD, P., and WONG T.-F. (2004), *Compaction, dilatancy and failure in porous carbonate rocks,* J. Geophys. Res. *109*, B10406, doi: 10.1029/2003JB002942.

VAJDOVA, V., CHEN, T.-M.N., and WONG, T.-F. (2006), *Micromechanics of the brittle-ductile transition in Tavel and Indiana limestones*, EOS Trans. AGU *87*(52), Fall Meeting Suppl., Abstract T23D-0521.

WONG, T.-F., DAVID C., and ZHU, W. (1997), *The transition from brittle faulting to cataclastic flow in porous sandstones: Mechanical deformation*, J. Geophys. Res. *102*, 3009–3025.

WONG, T.-F. and BAUD, P. (1999), *Mechanical compaction of porous sandstone*, Oil Gas Sci. Tech. *54*, 715–727.

WONG, T.-F., BAUD, P., and KLEIN, E. (2001), *Localized failure modes in a compactant porous rock*, Geophys. Res. Lett. *28*, 2521–2524.

WU, X.-Y., BAUD, P., and WONG, T.-F. (2000), *Micromechanics of compressive failure and spatial distribution of anisotropic damage in Darley Dale sandstone*, Int. J. Rock Min. Sci. *37*, 143–160.

ZHANG, J., WONG, T.-F., and DAVIS, M.D. (1990), *Micromechanics of pressure induced grain crushing in porous rocks*, J. Geophys. Res. *95*, 341–352.

(Received August 9, 2008, revised December 8, 2008, accepted March 6, 2009)
Published Online First: May 20, 2009